

Shape Invariant 3D-Variational Autoencoder : Super Resolution in Turbulence flow

Anuraj Maurya

Indian Institute of Science, Bangalore, India

anurajmaurya@iisc.ac.in

Abstract—Deep learning provides a versatile suite of methods for extracting structured information from complex datasets, enabling deeper understanding of underlying fluid dynamic phenomena. The field of turbulence modeling, in particular, benefits from the growing availability of high-dimensional data obtained through experiments, field observations, and large-scale simulations spanning multiple spatio-temporal scales. This report presents a concise overview of both classical and deep learning-based approaches to turbulence modeling. It further investigates two specific challenges at the intersection of fluid dynamics and machine learning: the integration of multiscale turbulence models with deep learning architectures, and the application of deep generative models for super-resolution reconstruction

I. INTRODUCTION

Modeling turbulent flow fields remains a formidable challenge, particularly due to the difficulty in accurately capturing high-order spatio-temporal statistics, which arise from the inherently intermittent and chaotic nature of turbulence. While the Navier–Stokes equations offer a complete mathematical description of fluid motion, no general analytical solution exists for these equations in the turbulent regime. Numerical methods offer an avenue for approximate solutions; however, the computational cost of Direct Numerical Simulations (DNS) of the full three-dimensional Navier–Stokes equations becomes prohibitively high in practical engineering applications, especially when a wide spectrum of spatial and temporal scales must be resolved [1].

Efforts to address this complexity date back to the early 20th century. One of the foundational contributions came from Osborne Reynolds, who introduced the concept of Reynolds decomposition, wherein any instantaneous quantity is decomposed into its mean and fluctuating components. This led to the development of the Reynolds-Averaged Navier–Stokes (RANS) equations, which remain a cornerstone in turbulence modeling.

The Reynolds-Averaged Navier–Stokes (RANS) equations describe the behavior of the mean flow by time-averaging the Navier–Stokes equations. They are written as:

$$\begin{aligned} \frac{\partial(\rho U_i)}{\partial t} + \frac{\partial(\rho U_i U_j)}{\partial x_j} = -\frac{\partial P}{\partial x_i} \\ + \frac{\partial}{\partial x_j} \left[\mu \left(\frac{\partial U_i}{\partial x_j} + \frac{\partial U_j}{\partial x_i} \right) - \rho \overline{U'_i U'_j} \right] \end{aligned} \quad (1)$$

Here, U_i and U_j denote the components of the mean velocity field, ρ is the fluid density, μ is the dynamic viscosity, and P is the mean pressure. The term $\rho \overline{U'_i U'_j}$ represents the *Reynolds stress tensor*, which emerges from averaging the nonlinear convective terms and encapsulates the effects of turbulence.

To solve the RANS equations, the Reynolds stress tensor must be modeled in terms of the mean flow quantities — a requirement known as the *turbulence closure problem*. This challenge has led to the development of numerous turbulence models, ranging from algebraic models to sophisticated multi-equation models, all aiming to approximate the turbulent (or eddy) viscosity and provide closure to the system.

A. Reynolds-Averaged Navier–Stokes (RANS) Model

Reynolds-Averaged Navier–Stokes (RANS) models are among the most widely used approaches for turbulence modeling in engineering applications due to their balance of computational efficiency and reasonable accuracy. RANS models work by decomposing instantaneous quantities into mean and fluctuating components and averaging the Navier–Stokes equations over time, resulting in the Reynolds stress terms that require additional modeling — known as the turbulence closure problem. Several turbulence models have been developed to approximate the Reynolds stress, the most notable among them being the k - ϵ model and the Spalart–Allmaras model.

1) k - ϵ Model [1]: The k - ϵ model is a two-equation eddy-viscosity model that introduces two transport equations to close the RANS equations: one for the turbulent kinetic energy (k), and another for its rate of dissipation (ϵ). It assumes isotropic turbulence and models the turbulent viscosity μ_t as a function of k and ϵ :

$$\mu_t = \rho C_\mu \frac{k^2}{\epsilon}$$

Transport equation for turbulent kinetic energy k :

$$\frac{\partial(\rho k)}{\partial t} + \nabla \cdot (\rho \mathbf{U} k) = \nabla \cdot \left[\left(\mu + \frac{\mu_t}{\sigma_k} \right) \nabla k \right] + P_k + P_b - \rho \epsilon + S_k$$

Transport equation for turbulent dissipation rate ϵ :

$$\frac{\partial(\rho \epsilon)}{\partial t} + \nabla \cdot (\rho \mathbf{U} \epsilon) = \nabla \cdot \left[\left(\mu + \frac{\mu_t}{\sigma_\epsilon} \right) \nabla \epsilon \right] + C_{1\epsilon} \frac{\epsilon}{k} (P_k + P_b) - C_{2\epsilon} \rho \frac{\epsilon^2}{k} + S_\epsilon$$

This model is robust and works well for free shear flows such as jets and mixing layers. However, its performance degrades in flows with strong pressure gradients, curvature effects, or near-wall flows without fine mesh resolution.

2) *Spalart–Allmaras Model [2]*: The Spalart–Allmaras (SA) model is a one-equation turbulence model designed specifically for aerospace applications involving wall-bounded flows, such as boundary layers under adverse pressure gradients. It introduces a new working variable $\tilde{\nu}$ rather than solving directly for the turbulent viscosity ν_t , thereby simplifying the computational cost while retaining reasonable physical fidelity.

Turbulent viscosity relation:

$$\nu_t = \tilde{\nu} f_{v1}, \quad f_{v1} = \frac{\chi^3}{\chi^3 + C_{\nu1}^3}, \quad \chi = \frac{\tilde{\nu}}{\nu}$$

Here, f_{v1} models the viscous damping effects, and the eddy viscosity is computed as $\mu_t = \rho\nu_t$.

Transport equation for $\tilde{\nu}$:

$$\begin{aligned} \frac{\partial \tilde{\nu}}{\partial t} + \nabla \cdot (\mathbf{U}\tilde{\nu}) = & C_{b1}\bar{S}\tilde{\nu} + \frac{1}{\sigma} \left[\nabla \cdot ((\nu + \tilde{\nu})\nabla\tilde{\nu}) \right. \\ & \left. + C_{b2}(\nabla\tilde{\nu})^2 \right] - C_{w1}f_{w1} \left(\frac{\tilde{\nu}}{d} \right)^2 \end{aligned} \quad (2)$$

This model eliminates the need to resolve the fine near-wall mesh required by two-equation models in the viscous sublayer. It is especially efficient for external aerodynamic simulations and has shown excellent performance in flows over airfoils, fuselages, and nozzles.

B. Large Eddy Simulation (LES) Model [1]

Turbulent flows consist of eddies of varying sizes and energies. LES models resolve the large-scale eddies directly and model the effects of smaller, unresolved eddies using a sub-grid scale (SGS) model. In contrast to RANS models, which do not resolve any turbulent fluctuations, LES explicitly captures a significant portion—typically 80% or more—of the turbulent kinetic energy (TKE).

The total turbulent kinetic energy (K) is decomposed as:

$$K = K_{res} + K_{sgs}$$

where K_{res} is the kinetic energy of the resolved eddies, and K_{sgs} represents the kinetic energy associated with sub-grid scale eddies (i.e., eddies smaller than the computational mesh). The SGS turbulent kinetic energy depends on the choice of the SGS model.

The *integral length scale* (l_0) denotes the size of the largest energy-containing eddies. The *sub-grid length scale* (l_{sgs}) corresponds to the eddy size with energy equal to the average of all unresolved eddies.

Turbulent eddies undergo a cascade process, transferring energy from large to small scales. Eventually, the smallest eddies are dissipated into heat via molecular viscosity. However, in LES, the smallest resolved eddies may not be adequately damped due to limited physical viscosity. This causes energy

buildup unless additional artificial dissipation is introduced via the SGS model. The effective dissipation rate is increased to:

$$\epsilon_{eff} = (\nu + \nu_{sgs}) \frac{\partial U_i \partial U_i}{\partial x_j \partial x_j}$$

where ν_{sgs} is the artificial viscosity introduced to mimic energy dissipation.

Sub-grid Stress:

To model energy transfer from resolved to unresolved scales, an additional SGS stress term τ_{sgs} is introduced:

$$\frac{\partial \rho}{\partial t} + \frac{\partial \rho U_j}{\partial x_j} = 0$$

$$\frac{\partial(\rho U_i)}{\partial t} + \frac{\partial(\rho U_i U_j)}{\partial x_j} = -\frac{\partial P}{\partial x_i} + \frac{\partial}{\partial x_j} (\tau_{ij} + \tau_{sgs})$$

The SGS stress acts as a resistive force, facilitating dissipation of eddies just above the mesh cutoff. It is commonly modeled using an eddy-viscosity hypothesis:

$$\begin{aligned} \tau_{sgs} = & 2\rho\nu_{sgs}S_{ij}^* - \frac{2}{3}\rho K_{sgs}\delta_{ij} \\ S_{ij}^* = & \frac{1}{2} \left(\frac{\partial \bar{U}_i}{\partial x_j} + \frac{\partial \bar{U}_j}{\partial x_i} - \frac{1}{3} \frac{\partial \bar{U}_k}{\partial x_k} \delta_{ij} \right) \end{aligned}$$

where S_{ij}^* is the trace-free strain rate tensor of the resolved velocity field.

C. Variational Multiscale (VMS) Model

[3]

In traditional LES, eddy diffusion impacts all scales of motion, often overdamping the resolved large scales and causing commutation errors. The Variational Multiscale (VMS) model addresses this by explicitly separating the governing equations into components for large (resolved) and small (unresolved) scales, with interaction terms that couple them. This separation enables a more accurate representation of sub-grid effects.

Smooth Case:

We consider a linear partial differential equation defined on an open, bounded domain $\Omega \subset \mathbb{R}^d$, with $d \geq 1$, and a smooth boundary $\Gamma = \partial\Omega$:

$$\mathcal{L}(u) = f \quad \text{in } \Omega, \quad u = g \quad \text{on } \Gamma,$$

where $f: \Omega \rightarrow \mathbb{R}$ and $g: \Gamma \rightarrow \mathbb{R}$. The variational formulation is given by:

$$(\mathcal{L}(u), w) = (f, w) \quad \text{for all } w \in \mathcal{V}, \quad u \in \mathcal{V}.$$

We decompose the solution and test function spaces:

$$\mathcal{V} = \mathcal{V}_h + \mathcal{V}'$$

Applying the VMS framework yields a system of coarse (resolved) and fine (unresolved) scale equations (assuming linear \mathcal{L}):

$$(\mathcal{L}(u_h), w_h) + (\mathcal{L}(u'), w_h) = (f, w_h)$$

$$(\mathcal{L}(u'), w') = -(\mathcal{L}(u_h) - f, w')$$

The fine-scale Green's function $g'(x, y)$ corresponding to the adjoint operator \mathcal{L}^* satisfies:

$$\Pi' \mathcal{L}^*(g'(x, y)) = \Pi'(\delta(x-y)), \quad \forall x \in \Omega, \quad g'(x, y) = 0 \text{ on } \Gamma$$

The fine-scale solution is obtained via superposition:

$$u'(y) = - \int_{\Omega} g'(x, y)(\mathcal{L}u_h - f)(x) d\Omega_x$$

Rough Case:

When derivatives are discontinuous across element boundaries (as in finite element methods), distributional effects must be explicitly accounted for. Here, piecewise continuous polynomial basis functions are used.

The fine-scale solution becomes:

$$u'(y) = - \sum_e \left(\int_{\Omega_e} g'(x, y)(\mathcal{L}u_h - f)(x) d\Omega_x + \int_{\Gamma_e} g'(x, y)(bu_h)(x) d\Gamma_x \right) \quad (3)$$

Applying a projection operator Π_f yields:

$$\Pi_f u'(y) = - \sum_e \left(\int_{\Omega_e} \Pi_f g'(x, y)(\mathcal{L}u_h - f)(x) d\Omega_x + \int_{\Gamma_e} \Pi_f g'(x, y)(bu_h)(x) d\Gamma_x \right) \quad (4)$$

D. Machine Learning Models for Turbulence Modeling

Traditional turbulence modeling in fluid dynamics—whether in Reynolds-Averaged Navier–Stokes (RANS) simulations or Large-Eddy Simulations (LES)—requires mathematical closures for unresolved quantities. Specifically, RANS models necessitate approximating the Reynolds stress tensor, while LES models focus on subgrid-scale (SGS) effects. However, even LES, which resolves large-scale motions, still relies on SGS models that may fall short in capturing fine-scale dynamics essential for certain applications. In recent years, machine learning (ML) approaches have emerged as promising alternatives by leveraging high-fidelity turbulence databases to infer statistical flow features and provide data-driven closures.

One of the earliest successful applications of ML in turbulence modeling was by Milano and Koumoutsakos [4], who used neural networks to reconstruct near-wall turbulent velocity fields. Although this work initially received limited attention, the rise of deep learning has revitalized interest in such approaches. For example, Lapeyre et al. [5] utilized

convolutional neural networks (CNNs) to model subgrid-scale reaction rates, and Fukami et al. [6] developed a CNN-based synthetic turbulence generator for inflow boundary conditions.

Zhang and Duraisamy [7] applied neural networks to infer spatially varying correction factors in turbulence models for both turbulent and transitional regimes. Ling et al proposed a deep neural network (DNN) framework to model the Reynolds stress anisotropy tensor, embedding Galilean invariance directly into the network architecture. Similarly, Kutz [8] demonstrated the effectiveness of DNNs compared to conventional RANS-based models, emphasizing the potential of deep learning in turbulence closure modeling.

Recent advances have also explored using ML for super-resolution of turbulent flows. Fukami et al. [9] employed deep CNNs to reconstruct high-resolution flow fields from coarse-grained 2D data. Their model was based on the Super-Resolution Convolutional Neural Network (SRCNN) architecture developed by Dong et al. [10], originally designed for image enhancement tasks. While effective for 2D flows, the applicability of these models to three-dimensional (3D) turbulence—where vortex stretching plays a critical role—remains an open question.

To address limitations in resolution, significant work has been done to enhance super-resolution networks [11]–[13]. However, standard CNN-based approaches often struggle with large upscaling factors and the recovery of high-wavenumber components. To overcome these issues, Ledig et al. [14] introduced the Super-Resolution Generative Adversarial Network (SRGAN), which uses a generative adversarial network (GAN) architecture. GANs, introduced by Goodfellow et al. [15], consist of two competing networks—a generator and a discriminator—trained simultaneously to produce increasingly realistic outputs.

Building upon this, Wang et al. applied SRGAN-based frameworks to enrich low-resolution 3D turbulence fields. In parallel, Variational Autoencoders (VAEs)—a class of generative models based on variational Bayesian inference—have also been proposed for turbulence modeling. VAEs, introduced by Kingma and Welling, consist of an encoder-decoder architecture that learns a probabilistic latent space and optimizes a reconstruction loss regularized by the Kullback-Leibler divergence between the approximate and true posterior distributions.

In this work, we propose two novel architectures: SR-3DGAN and SR-3DVAE, tailored for super-resolving three-dimensional turbulent flow fields. These models aim to bridge the gap between physics-informed turbulence modeling and high-resolution data synthesis. In future extensions, we plan to incorporate multiscale modeling capabilities to further enhance the accuracy and physical consistency of our predictions.

II. RELATED WORK

The paper by Deng et al. [16] developed a general GAN-based approach that reconstructs the high spatial resolution of turbulent flow fields, which helps obtain finer structures in turbulence. They used SRGAN and ESRGAN, which address

super-resolution problems due to their special network architectures and perceptual loss functions.

In contrast to the traditional pixelwise MSE loss, the perceptual loss in SRGAN comprises a content loss and an adversarial loss. Minimizing the MSE loss alone often results in overly smooth images lacking high-frequency content. The content loss, referred to as ‘‘VGG loss,’’ is obtained using a pre-trained VGG-19 network and evaluates the feature differences between real and generated images.

While the original SRGAN used RGB images as input, in their study, the model used 2D turbulent flow fields for super-resolution. The input includes (u, v, s) , where u is the streamwise velocity (x-velocity), v is the spanwise velocity (y-velocity), and s is the velocity magnitude. Given a low-resolution (LR) velocity field, the generator produces a high-resolution (HR) velocity field.

Two experimental setups were considered: flow around a single cylinder and flow behind two side-by-side cylinders. Experimentally generated data was used for both training and testing. The spatial resolution of velocity fields could be increased by factors of 4^2 and 8^2 using these networks. The generated velocity fields closely matched the ground truth.

The paper by Xu et al. [17] demonstrated the superiority of the 3D-SR-GAN network over direct interpolation methods for 3D turbulent jet flame structures. Their network used 3D convolution, skip connections, and an additional adversarial loss to capture high-frequency details.

3D volumetric flame data were generated using Large Eddy Simulation (LES) of a turbulent piloted CH_4/air diffusion flame (Sandia flame B and C). The simulations solved reactive Navier–Stokes equations with a 16-component CH_4/air chemical mechanism using the finite volume method. A small timestep (10^{-5} s) was used to resolve the flame dynamics.

3D-SR-GAN upscaled the turbulent flame structure by a factor of two in all spatial directions with high fidelity. It outperformed traditional interpolation methods both quantitatively and qualitatively.

Subramaniam et al. [18] proposed the TEResNet and TEGAN models, which outperformed simple tricubic interpolation for upsampling turbulent data. Data was generated using an in-house CFD simulation with spectral spatial discretization and a third-order TVD Runge–Kutta scheme. DNS simulations on a $64 \times 64 \times 64$ grid produced snapshots of velocity and pressure fields. Low-resolution data was created by filtering down to $16 \times 16 \times 16$.

The generator’s loss function combined content loss and a physics-based loss, including residuals of the continuity and pressure Poisson equations. This ensured physically consistent outputs. TEGAN and TEResNet enriched low-resolution turbulence data and added fine-scale features to recover DNS-level fidelity. TEGAN captured physics better and generalized well to test data.

Pradhan et al. [19] proposed a VMS-inspired approach incorporating feature selection, VMS-consistent closure, and a physics-informed network architecture.

They assumed a coarse space composed of piecewise linear

polynomials and governed by a linear convection-diffusion equation:

$$\mathcal{L} = a \frac{d}{dx} - \kappa \frac{d^2}{dx^2}, \quad \text{in } \Omega = [0, L], \quad u = 0 \text{ on } \Gamma = \{0, L\}$$

For a 1D element of size h , the coarse solution u_h is expressed as:

$$u_h(x) = u(0) \left(1 - \frac{x}{h}\right) + u(h) \left(\frac{x}{h}\right)$$

The fine-scale space is a discontinuous finite element space. The L_2 -optimal approximation of the fine scales u' in an element is:

$$\Pi_f u'(y) = \int_{\Omega_e} \Pi_f(g'(x, y)) a \left(\frac{u(h) - u(0)}{h}\right) d\Omega_x$$

Assuming Dirichlet boundary conditions at endpoints, the exact sub-scale is:

$$u'(y) = (u(h) - u(0)) \left(\frac{1 - e^{-\frac{2\alpha y}{h}}}{1 - e^{-2\alpha}} - \frac{y}{h}\right)$$

Approximating this in a discontinuous p_0 space gives:

$$u'_0(y) = (u(h) - u(0)) \cdot \frac{h}{2\alpha} \left(\coth(\alpha) - \frac{1}{\alpha}\right)$$

Defining element-level mean and RMS quantities:

$$u_m = \frac{1}{h} \int_0^h u_h d\Omega, \quad u_{rms} = \sqrt{\frac{1}{h} \int_0^h (u_h - u_m)^2 d\Omega}$$

The normalized sub-scale form is:

$$\frac{u'_0(y)}{u_{rms}} = \sqrt{3} \left(\frac{1}{\alpha} - \coth(\alpha)\right) \text{sign}(u(h) - u(0))$$

Hence,

$$\frac{u'_0(y)}{u_{rms}} = f\left(\alpha, \frac{u(h) - u(0)}{u_{rms}}\right)$$

Data was generated by solving the equation for different Péclet numbers on fine meshes. The coarse-scale interpolant and corresponding sub-scale were computed for each element. The optimal sub-scale in a discontinuous $p = 1$ basis is given as:

$$\frac{u'_0(y)}{u_{rms}} = C'_1(\alpha)\psi_1\left(\frac{y}{h}\right) + C'_2(\alpha)\psi_2\left(\frac{y}{h}\right)$$

and the function to be learned is:

$$[C'_1, C'_2] = f(\alpha)$$

This idea extends to both linear and nonlinear problems using discontinuous basis functions. The final super-resolved solution is:

$$u_{sr} = u_{pc} + u'_{ps} = u_{pc} + u_{rms} \sum_i^{(p_s+1)^d} C'_{i,p_s} \psi_{i,p_s}$$

The model inputs include physics-informed parameters and normalized coarse-scale coefficients from neighboring elements. Two architectures are used:

- Traditional NN: $u' = f^{FNN}(\alpha, u_c)$

- **VSRNN**: $u' = f^{FNN}(g_\alpha \odot g_u)$, where $g_\alpha = h^{FNN}(\alpha)$ and $g_u = k^{FNN}(u_c)$, with \odot denoting element-wise multiplication.

This approach allows the network to learn physically consistent fine-scale reconstruction from coarse data.

III. METHODOLOGY

A. Johns Hopkins Turbulence Database (JHTDB)

Turbulent Channel Flow : This dataset is generated from direct numerical simulation (DNS) of wall-bounded turbulent flow with no-slip boundary conditions at the top and bottom walls, and periodic boundary conditions in the streamwise (x) and spanwise (z) directions [20]. The simulation solves the incompressible Navier–Stokes equations using a velocity–vorticity formulation in the wall-normal direction. A Fourier–Galerkin pseudo-spectral method is applied in the streamwise and spanwise directions, while seventh-order basis-spline (B-spline) collocation is used in the wall-normal direction.

Temporal integration is performed using a low-storage third-order Runge–Kutta scheme. The simulation is initially driven by imposing a unit bulk channel mean velocity until a statistically stationary state is reached. Thereafter, a constant mean pressure gradient is applied to maintain the flow. Three-component velocity and pressure fields are saved every five time steps, resulting in 4000 time-resolved data frames. The simulation setup used for DNS is summarized in Table I.

TABLE I
DNS SIMULATION PARAMETERS (JHTDB)

Parameter	Value
Domain Dimensions	$8\pi \times 2 \times 3\pi$
Grid Resolution	$2048 \times 512 \times 1536$
DNS Time Step	0.0013
Data Saved Every	0.0065 time units
Total Time Span	[0, 25.9935]

Note: The DNS data used is from the Johns Hopkins Turbulence Database (JHTDB). Values represent simulation settings for the isotropic turbulence dataset.

B. Oasis-Based Channel Flow Simulation

To complement the DNS data, we performed large-eddy simulation (LES) of turbulent channel flow using the Oasis solver. The simulation domain and boundary conditions mimic those of JHTDB: the flow is confined between two parallel walls and is periodic in the streamwise and spanwise directions. A constant pressure gradient drives the flow in the streamwise (x) direction. The simulation setup used for LES is summarized in Table II.

C. Dataset Preparation for Deep Learning Models

To train the deep learning models, we extract high-fidelity three-dimensional (3D) velocity field data from the DNS of channel flow at two distinct time steps: **3200** for training

TABLE II
LES SIMULATION PARAMETERS (OASIS)

Parameter	Value
Domain Dimensions	$8\pi \times 2 \times 3\pi$
Coarse/Fine Grid	$160 \times 120 \times 40$
LES Time Step	0.005
Output Frequency	Every 0.1 time units
Total Time Span	[0, 25]

Note: The LES simulations were performed using the Oasis solver. Grid resolution and output frequency are configured for reduced computational cost while capturing essential dynamics.

and **3280** for testing. These time steps correspond to fully developed turbulence conditions, ensuring that the dataset contains complex and realistic flow structures.

Patch-Based Sampling Approach: Super-resolving the entire domain in one go is computationally infeasible for large-scale turbulent flows. To address this, we adopt a **localized patch-based approach**, where small 3D sub-volumes (cubes) of the flow field are extracted and processed independently.

We define a cube of size (q, q, q) and slide it over the entire domain with a stride of s in all three directions (x, y, z). The stride s determines how far the cube moves between samples and is selected based on computational resources and the desired resolution.

Downsampling and Coarsening Strategy: We introduce a coarsening factor A to control the resolution of low-resolution inputs. The cube size q is then defined as:

$$q = A \cdot s$$

This ensures that downsampling the original cube with a stride of A yields a **low-resolution (LR)** cube of size $(16, 16, 16)$.

The corresponding **high-resolution (HR)** target is constructed by extracting the central $(16, 16, 16)$ region of the original full-resolution cube. This ensures spatial alignment between the LR input and HR target and avoids edge effects.

a) *Example:*: Let $A = 4$ and $s = 4$, then:

$$q = 4 \cdot 4 = 16$$

- A cube of size $(16, 16, 16)$ is extracted from the full-resolution DNS data.
- The LR input is formed by downsampling the cube using a stride of $A = 4$, resulting in a $(4, 4, 4)$ cube, which is then upsampled to $(16, 16, 16)$.
- The HR output is the central $(16, 16, 16)$ portion of the original cube.

Velocity Components and Temporal Separation: Each point in the DNS velocity field includes three velocity components (u, v, w) representing streamwise, wall-normal, and spanwise directions. For simplicity, we use only the **streamwise component** (u) in this study, which aligns with the primary flow direction in the channel.

To prevent temporal leakage and ensure model generalization, we use:

- **Timestamp 3200** for generating training samples
- **Timestamp 3280** for testing

This temporal separation ensures unbiased evaluation of the model on unseen turbulent flow structures.

D. Data-Driven Models

TABLE III
ARCHITECTURE OF 3D-GAN GENERATOR

Layer	Details
Input	Concatenation of two inputs
Conv3D-1	Kernel 3, LeakyReLU
Conv3D-2	Kernel 3, BN, LeakyReLU
Conv3D-3	Kernel 3, BN, LeakyReLU
Conv3D-4	Kernel 3, BN, LeakyReLU
Conv3D-5	Kernel 3, BN, LeakyReLU
Conv3D-6	Kernel 3, Activation

Note: BN = Batch Normalization. Activation at the end is typically \tanh or sigmoid . All Conv3D layers use padding=same.

TABLE IV
3D-GAN DISCRIMINATOR ARCHITECTURE

Layer(s)	Description
Input	$D \times H \times W \times C$ volume
Conv3D \times 5	Kernel 3, BN, LeakyReLU
Conv3D	Kernel 3, Activation
Deconv3D \times 4	Kernel 3, BN, Activation
Output	Deconv3D, final activation

Note: BN = Batch Normalization. *Deconv3D* = Conv3DTranspose. All layers use padding='same'. Final activation is typically sigmoid (binary) or linear (WGAN).

1) *3D-GAN Model:* The 3D-GAN is a conditional generative adversarial network designed to perform super-resolution on coarse 3D flow data. The network architecture is illustrated in table III, IV. Given a coarse-resolution 3D input of size (16, 16, 16), the generator is trained to produce a fine-resolution output of the same spatial dimensions.

The generator adopts a U-Net-like structure composed of multiple blocks of 3D convolution, batch normalization, and ReLU activations, followed by corresponding transpose 3D convolution layers. Skip connections are used to concatenate features from encoder layers to decoder layers, preserving spatial information across scales.

The discriminator is trained to distinguish between real fine-resolution outputs and those generated by the generator. To stabilize the adversarial training and avoid mode collapse, we use the Wasserstein loss with gradient clipping, as proposed by [21].

2) *3D-VAE Model:* The 3D-VAE model consists of a 3D encoder, a latent embedding space, and a 3D decoder. The architecture is illustrated in table V and VI. The input to the encoder is a cube of dimensions (16, 16, 16). This input is

TABLE V
3D-VAE ENCODER ARCHITECTURE

Layer	Details
Input	$D \times H \times W \times C$ volume
Conv3D-1	32 filters, $k=3$, $s=1$
Conv3D-2	64 filters, $k=3$, $s=2$
Conv3D-3	128 filters, $k=3$, $s=2$
Conv3D-4	256 filters, $k=3$, $s=2$
Flatten	Vectorize output
Dense-1	Fully connected layer
Dense- μ	Latent mean μ
Dense-log σ^2	Latent log-var
Latent z	$\mu + \sigma \cdot \epsilon$

Note: All Conv3D and Dense layers use BatchNorm and ReLU unless noted. $\sigma = \exp(0.5 \cdot \log \sigma^2)$.

TABLE VI
3D-VAE DECODER ARCHITECTURE

Layer	Details
Input	Latent vector z
Dense-1	Expand z to 3D shape
Reshape	3D tensor for decoding
ConvT-1	256 filters, $k=3$, $s=2$
ConvT-2	128 filters, $k=3$, $s=2$
ConvT-3	64 filters, $k=3$, $s=2$
ConvT-4	32 filters, $k=3$, $s=1$
ConvT-5	Output layer (linear/sigmoid)

Note: All ConvTranspose layers use BatchNorm and ReLU, except the final layer.

passed through a series of 3D convolutional layers with batch normalization, reducing the spatial dimensions to (3, 3, 3).

The resulting volume is flattened into a (27, 1) vector and passed through a fully connected layer to obtain a (16, 1) latent representation. This latent dimension is treated as a hyperparameter and was selected through empirical tuning based on training performance.

The encoder outputs the mean and variance vectors of a Gaussian distribution, from which a latent variable λ of size (16, 1) is sampled. This sampled latent variable is then passed through the decoder, which consists of a fully connected layer, reshaping operation, and a sequence of 3D transpose convolution layers to reconstruct the original spatial resolution of (16, 16, 16).

The model was trained using only one velocity component at a time (e.g., the streamwise u -component). Separate models were trained and saved for each of the three velocity components (u , v , w), using datasets derived from various coarsening levels described earlier.

Training and validation losses were observed to converge smoothly after hyperparameter tuning. To assess the model's super-resolution capability, we evaluated it on unseen samples from the test set corresponding to coarsening level 3. For

qualitative visualization, randomly selected planes (X-Y, Y-Z, or X-Z) from the predicted 3D velocity fields are plotted, along with the corresponding coarse input, high-resolution ground truth, and reconstruction error.

Results presented in this paper focus on the u -velocity component. The performance for other velocity components follows similar trends and is omitted for brevity.

IV. POST-PROCESSING

After generating the predicted fine-resolution flow field using trained models as shown in the figure 1 and 2, post-processing is carried out to reconstruct the complete fine-scale flow field throughout the turbulent channel domain. This step essentially reverses the data generation process described earlier, but in the opposite direction—converting localized super-resolved patches into a global field.

Reconstruction from Patches

During data generation, we divided the domain into overlapping 3D patches (or cubes) of size (q, q, q) using a sliding window with stride s . For each patch, the central region of size $(16, 16, 16)$ was used as the high-resolution target. In post-processing, we follow a consistent procedure: we slide the window over the coarse input domain using the same stride s and coarsening factor A as used during training.

Each input patch is passed through the super-resolution model (e.g., 3D-VAE), which outputs a fine-resolution cube. These fine-resolution outputs are then stitched together to reconstruct the global field. To reduce boundary artifacts and ensure smooth transitions, overlapping regions between patches are averaged. This technique helps in obtaining a seamless and coherent high-resolution prediction over the entire 3D domain.

Consistency with Data Generation

To maintain consistency and avoid misalignment between ground truth and prediction, it is essential to use the same values for cube size q , stride s , and coarsening factor A that were employed during dataset preparation. This ensures the reconstructed high-resolution domain aligns properly with the original DNS data.

Visualization and Evaluation

To qualitatively and quantitatively evaluate the super-resolved predictions, we compare the following:

- **Ground Truth DNS:** The original high-resolution DNS velocity field.
- **Coarse Input:** The downsampled (coarsened) input fed to the model.
- **Predicted Output:** The reconstructed fine-resolution velocity field obtained from the 3D-VAE model.
- **Reconstruction Loss:** The absolute or squared error between the predicted and ground truth fields.

In Fig. 9, we visualize these fields for a representative X-Y plane located at the midsection of the channel ($z = L_z/2$).

- 1) The coarse-resolution input velocity field.

- 2) The corresponding DNS ground truth.
- 3) The super-resolved prediction from the 3D-VAE.
- 4) The pixel-wise reconstruction error.

This comparison helps in evaluating the performance of the model in restoring fine-scale structures, particularly in near-wall and high-gradient regions where turbulence is most intense.

TABLE VII
COMPARISON OF VELOCITY IN X-DIR

Model	Min Amplitude	Max Amplitude
Coarse DNS	0.2995	1.9982
Actual DNS	0.1511	2.0627
3D-VAE	0.4242	2.0097
Loss (Amplitude)	0.6001	

Note: Amplitudes computed from simulation outputs; loss represents mean absolute difference in amplitude.

V. SPECTRAL ANALYSIS USING FAST FOURIER TRANSFORM (FFT)

To evaluate the fidelity of the super-resolved flow field beyond pointwise errors, we perform a spectral comparison using the Fast Fourier Transform (FFT). This analysis offers insight into how well the model captures the underlying frequency content and multi-scale structures of turbulence.

We compute the 2D FFT of the velocity field on an X-Y plane at the midsection ($z = L_z/2$) for three cases: the coarse-resolution DNS input, the ground-truth high-resolution DNS solution, and the 3D-VAE super-resolved prediction. The results are visualized as separate plots for amplitude and phase components at different coarsening scales.

Amplitude and Phase Analysis

Amplitude spectra represent the energy distribution across spatial frequencies. Accurately capturing the amplitude across a wide range of wavenumbers is critical for reproducing the correct turbulence energy cascade, from large-scale eddies to small-scale dissipative structures.

Phase spectra, on the other hand, provide insight into the spatial arrangement and coherence of flow structures. Even when amplitude matches, incorrect phase information can lead to spatial misalignment of features such as vortices, streaks, or shear layers.

Interpretation and Observations

From the FFT plots, we observe the following:

- The 3D-VAE model is able to recover most of the low- and mid-frequency modes, which correspond to large and intermediate-scale flow structures. This shows that the model captures the dominant energy-carrying features of turbulence.
- At very high-frequency modes (small-scale structures), some deviation from the DNS ground truth is observed. This is expected due to both the resolution limitation of

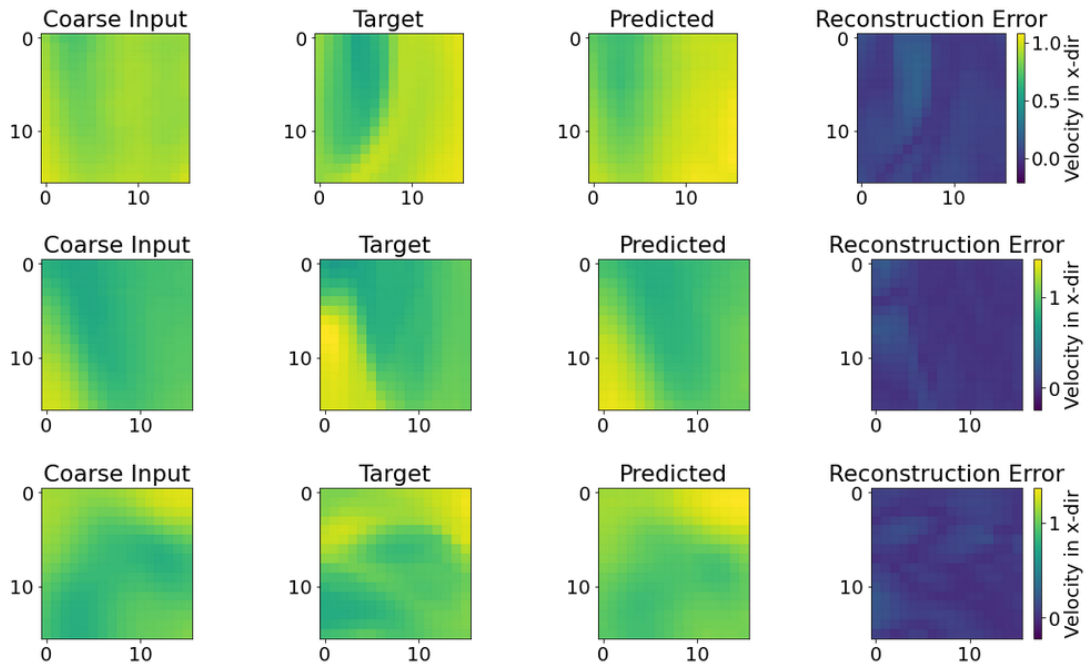


Fig. 1. 3D-GAN output

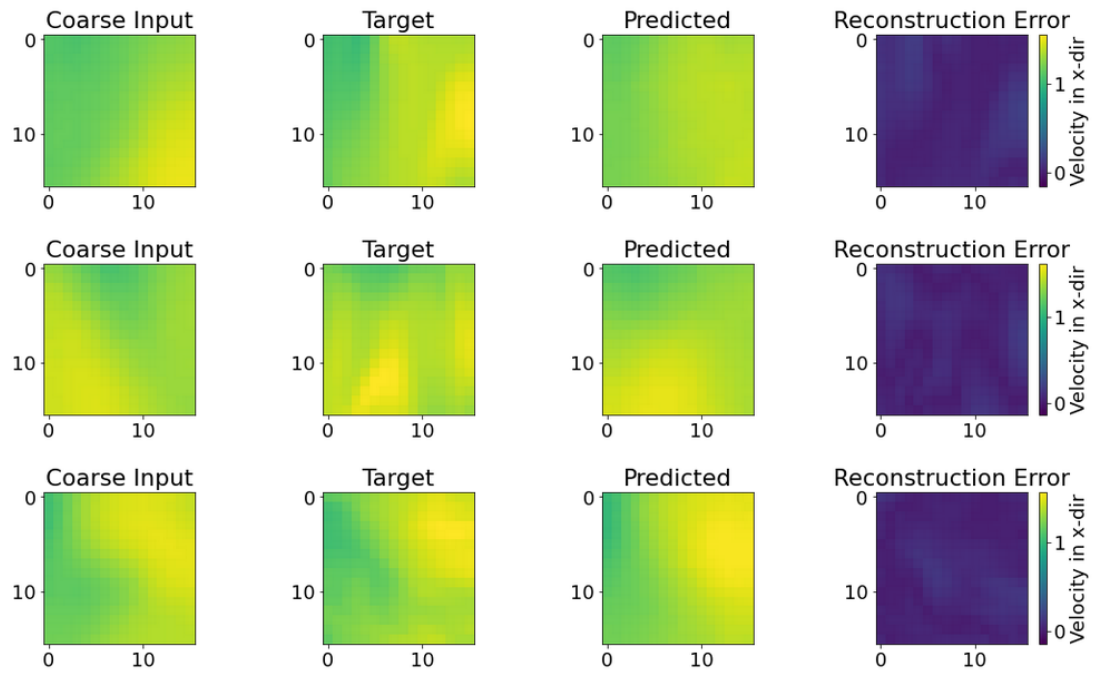


Fig. 2. 3D-VAE output

Fig. 3. Model predictions compared to ground truth across Z-X, Z-Y, and Y-X planes (top to bottom) for velocity in the x-direction.

TABLE VIII
FFT AMPLITUDE COMPARISON

Model	Min Amplitude	Max Amplitude
Coarse DNS	-3.41	8.99
Actual DNS	-7.50	12.91
3D-VAE	-5.40	12.92
Loss (Amplitude)	7.27	

Note: Amplitude range extracted from 2D FFT on the X-Y plane. Loss is mean absolute amplitude difference.

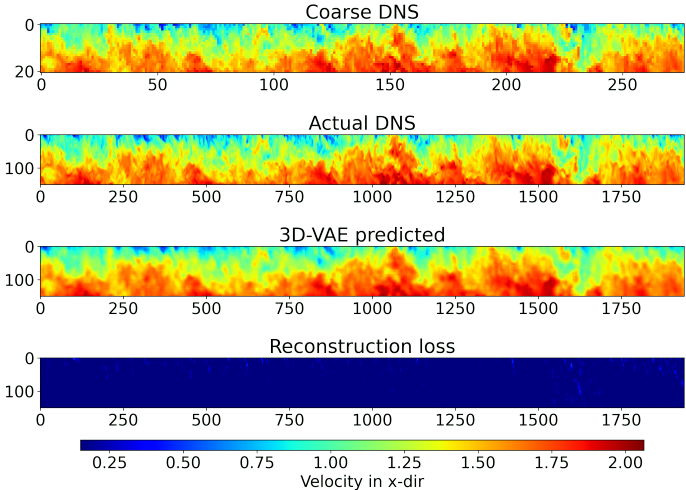


Fig. 4. Quantitative comparison of minimum and maximum velocity field values across the X-Y plane for different models.

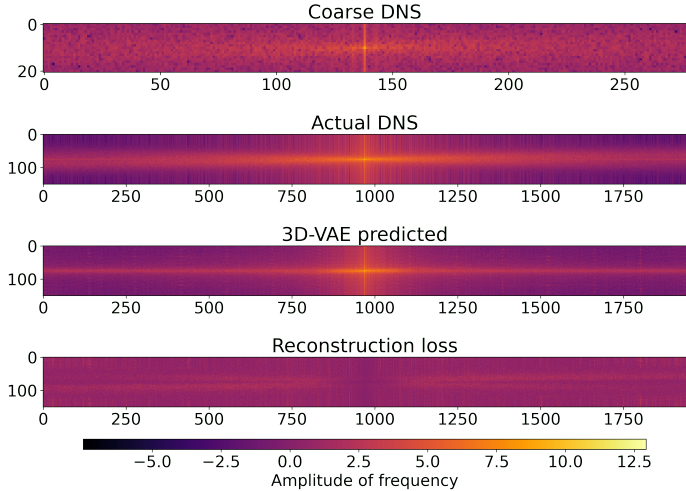


Fig. 5. FFT amplitude comparison across the X-Y plane for different models.

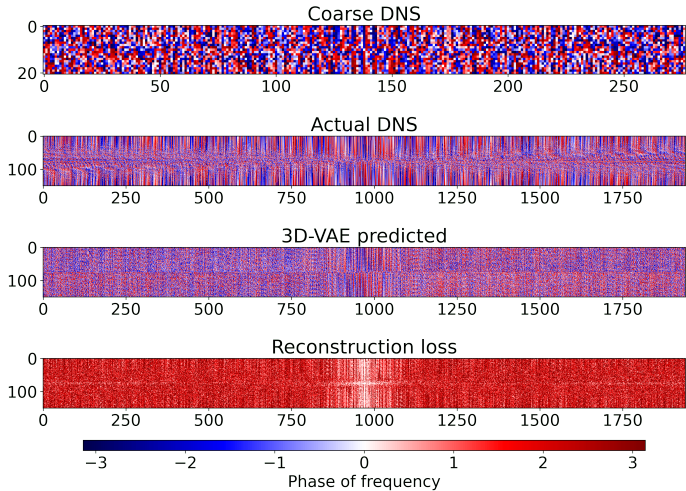


Fig. 6. FFT phase comparison across the X-Y plane for different models.

the input data and the intrinsic smoothing effect of neural networks.

- Periodic artifacts appear in the super-resolved output, which are visible as repeating patterns in the phase plots. These arise due to the use of fixed-size cubes (e.g., $16 \times 16 \times 16$) during patch-wise training and inference.
- Increasing the cube size reduces the strength of these artifacts by allowing the model to capture longer-range spatial correlations. However, this comes at the cost of increased memory usage and model complexity, requiring more training data and computational resources. Thus, there is a trade-off between resolution accuracy and practical feasibility.

Why Spectral Comparison is Important

Traditional pointwise metrics like Mean Squared Error (MSE) or L_2 -norms provide limited insight into how well the model captures multi-scale features of turbulence. Spectral analysis using FFT serves several key purposes:

- It quantifies how energy is distributed across scales, which is essential for validating models on turbulent flows governed by nonlinear interactions across frequencies.
- It reveals aliasing effects, spectral damping, or amplification that may not be visible in real-space metrics.
- It ensures that both the geometry (phase) and intensity (amplitude) of turbulent structures are preserved, which is crucial for downstream tasks like flow control or LES model development.

In summary, FFT-based amplitude and phase comparisons complement spatial-domain error metrics by offering a frequency-domain perspective of model performance. This ensures that the super-resolution model not only "looks right" in the real space but also "behaves right" in the spectral sense, which is vital for physically consistent predictions. As illustrated in figure 5 and 6

VI. COMPARISON WITH INTERPOLATION METHODS

To evaluate the effectiveness of our proposed 3D-VAE model, we compare its performance against two commonly used interpolation techniques: **cubic interpolation** and **Lanczos interpolation**. These methods serve as baseline approaches for enhancing coarse-resolution data without learning-based supervision.

We assess the performance both qualitatively and quantitatively. For quantitative analysis, we compute the **reconstruction loss** (mean squared error) between the super-resolved output and the ground truth DNS field. For qualitative analysis, we use the **2D Fast Fourier Transform (FFT)** to compare the spectral properties of the predicted fields on the X-Y midsectional plane.

Figure 7 and 8 shows:

- Reconstruction losses for cubic interpolation, Lanczos interpolation, and the 3D-VAE model.
- FFT amplitude plots for each method, providing insight into how well fine-scale features are recovered.

TABLE IX

MAXIMUM AND AVERAGE ERROR COMPARISON FOR VELOCITY IN X-DIR

Method	Max Error	Avg. Error
3D-VAE	0.6001	0.0547
Cubic	0.9433	0.0749
Lanczos	0.9589	0.0759

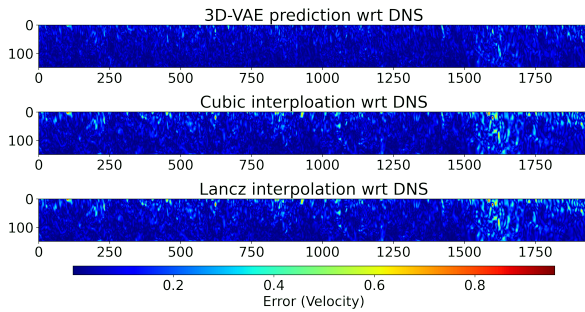


Fig. 7. Comparison of 3D-VAE solution with image interpolation methods.

TABLE X

MAXIMUM AND AVERAGE ERROR COMPARISON FOR FFT AMPLITUDE

Method	Max Error	Avg. Error
3D-VAE	7.2714	0.9062
Cubic	10.9714	2.6259
Lanczos	9.0570	2.8463

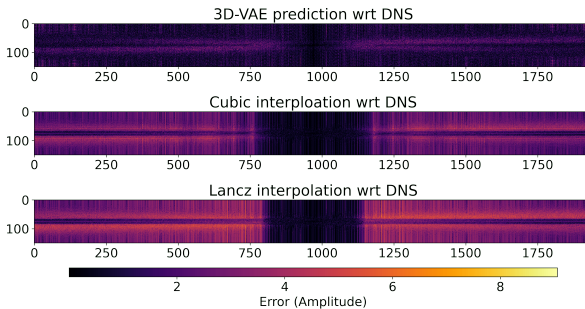


Fig. 8. FFT amplitude comparison of 3D-VAE solution with image interpolation methods.

The results show that:

- **3D-VAE significantly outperforms both interpolation methods** in terms of reconstruction loss, indicating better pixel-wise accuracy.
- FFT analysis reveals that the 3D-VAE preserves more high-frequency content, corresponding to fine-scale turbulent structures, which are otherwise smoothed out by the interpolation techniques.

This comparison confirms that data-driven deep learning models, such as 3D-VAE, are better suited for recovering physically meaningful flow features than traditional interpolation methods, particularly in complex turbulent flow fields.

VII. LES TO DNS SUPER-RESOLUTION

In this section, we demonstrate the application of the 3D-VAE model for super-resolving coarse-resolution LES (Large Eddy Simulation) data to DNS (Direct Numerical Simulation) fidelity. The dataset used here is consistent with that described in the simulation chapter to ensure comparability. Specifically, data snapshots were extracted at 20-second intervals for the training set and at 21-second intervals for the test set to avoid temporal overlap and ensure generalization.

The coarse LES data is defined on a spatial grid of (160, 120, 40), whereas the fine LES data has a higher resolution of (320, 240, 80). To prepare the training dataset, the fine-resolution field is downsampled to match the coarse grid, following the procedure outlined in the previous section. The 3D-VAE model is then trained to learn the mapping from low-resolution inputs to their corresponding high-resolution DNS.

Post-processing and Evaluation

TABLE XI

COMPARISON OF VELOCITY IN X-DIR OVER X-Y PLANE [COARSE LES]

Model	Min Value	Max Value
Coarse DNS	0.2290	0.6745
Actual DNS	0.6020	1.2664
3D-VAE	0.6118	1.1929
Loss (Max)	–	0.2118

Note: Min/Max values computed over X-Y plane. Loss indicates absolute difference in maximum value.

After inference, the predicted high-resolution velocity field from the 3D-VAE is post-processed to reconstruct the full turbulent channel flow at DNS resolution. For visualization and evaluation, we focus on the velocity component in the x -direction.

Figure 9 and 12 show the reconstruction results on the X-Y plane at the midsection. The comparison includes:

- The original coarse LES input.
- The ground truth DNS solution.
- The 3D-VAE super-resolved output.
- The reconstruction error map.

Similar results have been observed for the Y-Z and Z-X planes.

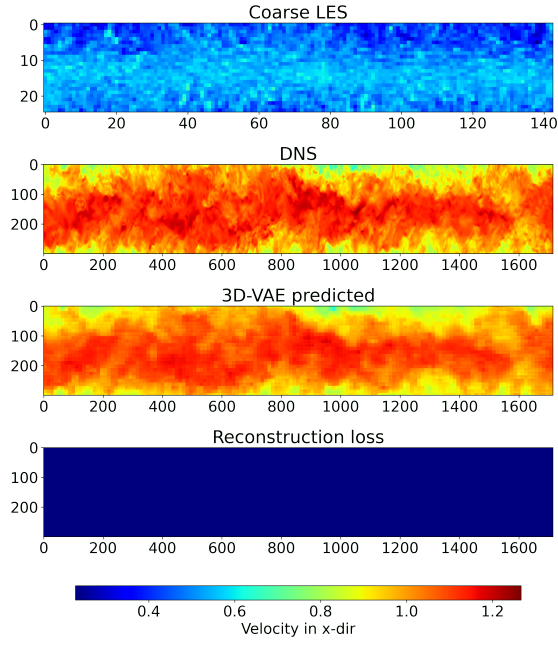


Fig. 9. Quantitative analysis [velocity in x-dir] over X-Y plane

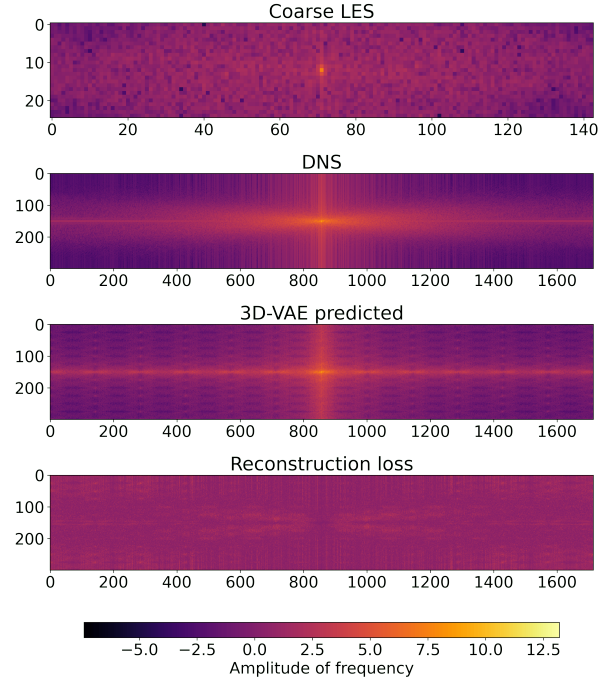


Fig. 10. Qualitative analysis over X-Y plane

Spectral Analysis via FFT

To further assess the fidelity of super-resolved predictions, we analyze the frequency spectrum of the velocity field using the 2D Fast Fourier Transform (FFT). We compute and compare both the amplitude and phase spectra for:

- Coarse LES input,
- Ground truth DNS,
- 3D-VAE predictions.

TABLE XII
MIN AND MAX VALUE COMPARISON (FFT, X-Y PLANE) [COARSE LES]

Model	Min Value	Max Value
Coarse LES	-4.5221	7.4949
DNS	-7.3919	13.1899
3D-VAE	-6.8298	13.1755
Loss (Max)	–	7.9236

TABLE XIII
COMPARISON OF VELOCITY IN X-DIR OVER X-Y PLANE [FINE LES]

Model	Min Value	Max Value
Fine LES	0.2622	0.6745
DNS	0.6349	1.2669
3D-VAE	0.7536	1.1398
Loss (Max)	–	0.2192

TABLE XIV
MIN AND MAX VALUE COMPARISON (FFT, X-Y PLANE) [FINE LES]

Model	Min Value	Max Value
Fine LES	-4.7658	8.9022
DNS	-7.1272	13.1889
3D-VAE	-7.0866	13.1835
Loss (Max)	–	7.2220

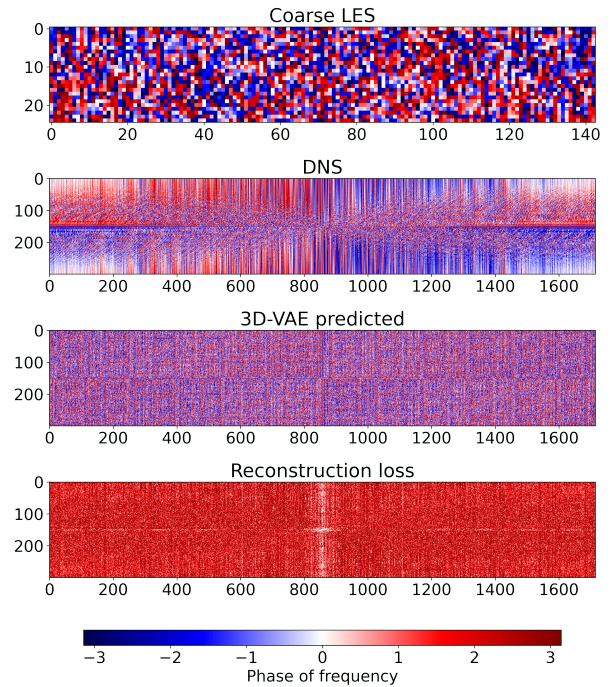


Fig. 11. Qualitative analysis over X-Y plane

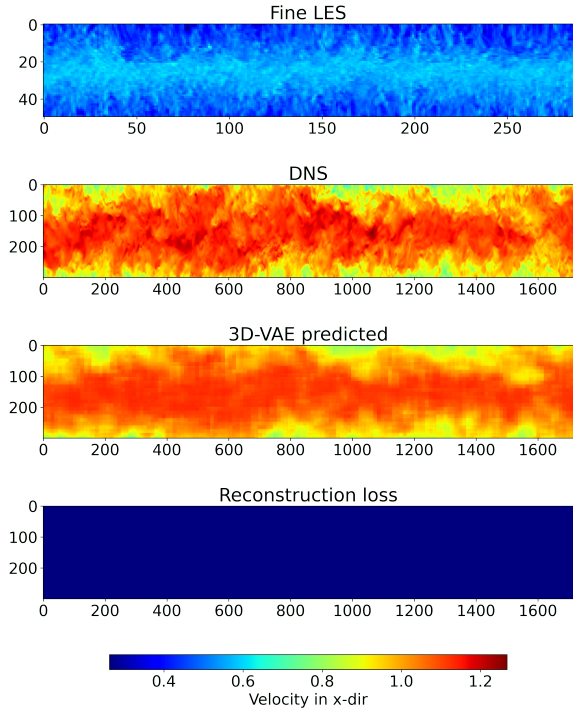


Fig. 12. Quantitative analysis [velocity in x-dir] over X-Y plane

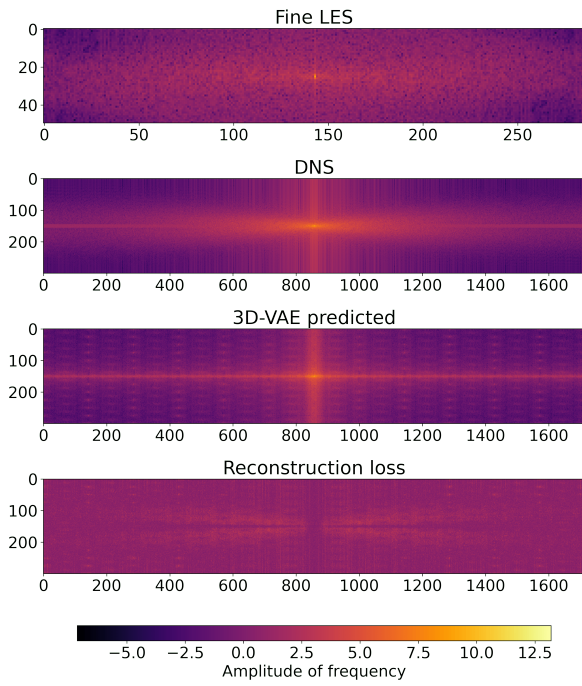


Fig. 13. Qualitative analysis over X-Y plane

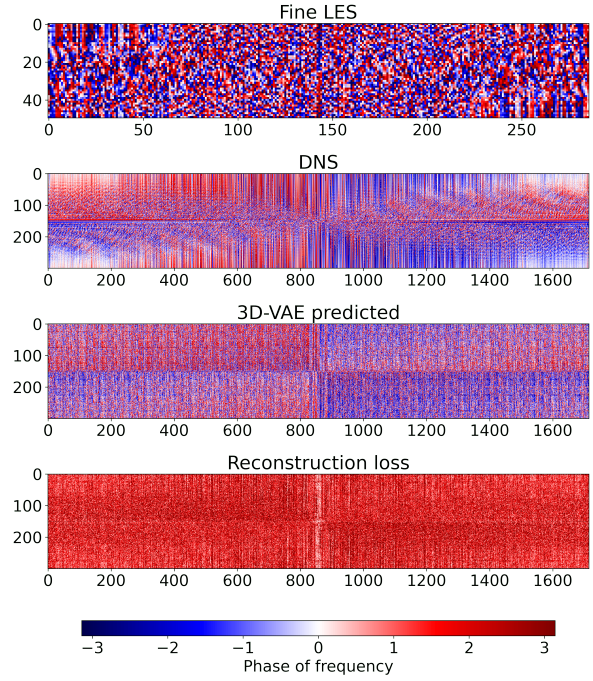


Fig. 14. Qualitative analysis over X-Y plane

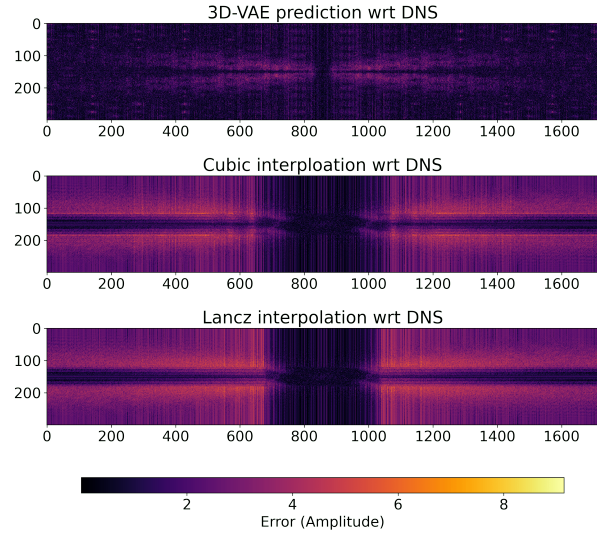


Fig. 15. Comparison of 3D-VAE solution with image interpolation method

TABLE XV
MAX AND AVERAGE ERROR COMPARISON (FFT, X-Y PLANE)

Method	Max Error	Average Error
3D-VAE	7.2220	0.9175
Cubic	9.0866	2.3293
Lancz	9.1416	2.5784

Figure 10, 11, 13 and 14 present the spectral plots for the X-Y midsectional plane. The results show that the 3D-VAE effectively recovers fine-scale structures and high-frequency modes that are absent in the LES input but present in the DNS

ground truth. This highlights the model’s capability to infer missing turbulent structures and generate physically realistic flow fields beyond traditional interpolation approaches.

VIII. CONCLUSION AND FUTURE WORK

Super-resolution of turbulent flow fields has been an active area of research, particularly for specific canonical cases and at relatively low Reynolds numbers. While deep generative models have shown promising results, existing approaches often face limitations in scalability due to the rapidly increasing number of model parameters when attempting to resolve larger spatial domains. This makes such models computationally prohibitive for practical fluid simulations.

To address this challenge, we proposed two deep learning architectures—3D-GAN and 3D-VAE—for super-resolution in three-dimensional turbulent flows. Our approach is based on the hypothesis that a coarse-resolution representation over a larger spatial context carries sufficient information to reconstruct a fine-resolution solution at the center of that region. This insight guided the design of our dataset generation strategy, which uses convolution-based sampling to ensure robustness across different flow shapes.

Among the two models, 3D-GAN did not perform satisfactorily on either training or test data, even with enhancements such as Wasserstein loss and gradient clipping. Future work on 3D-GAN will focus on incorporating physics-informed loss functions in combination with the reconstruction loss to improve convergence and physical fidelity.

On the other hand, 3D-VAE demonstrated strong performance on both training and test datasets. Notably, the model effectively reconstructs DNS-resolution flow fields using only coarse-resolution LES data. As the downsampling factor increases (e.g., halving resolution in each spatial dimension), the computational cost is significantly reduced—by approximately a factor of eight—while still maintaining reasonable reconstruction accuracy. Importantly, 3D-VAE does not merely interpolate; it learns the underlying distribution of the flow and reconstructs physically plausible structures at fine scales.

While the results are encouraging, challenges remain. The 3D-VAE model tends to smooth out small-scale eddies, and further work is needed to refine hyperparameters, improve the loss function, and expand the training dataset. Future studies should examine the scientific generalizability of the model—particularly whether a model trained on downsampled DNS data can generalize to low-resolution data generated using other numerical methods such as FEM or FVM.

We also plan to investigate the temporal consistency of 3D-VAE, aiming to extend the model for time-series predictions of turbulent flow evolution. Additionally, ongoing work on training the 3D-SRGAN model may offer improvements in capturing fine-scale structures. Once a robust model is established, we aim to integrate it within the Variational Multiscale (VMS) framework.

Currently, reconstructed flow fields are assembled by directly concatenating predicted cubes. Future work will also

explore developing deep learning-based models for post-processing and seamless stitching of local predictions into coherent global flow fields.

REFERENCES

- [1] S. B. Pope and S. B. Pope, *Turbulent flows*. Cambridge university press, 2000.
- [2] P. Spalart and S. Allmaras, “A one-equation turbulence model for aerodynamic flows,” in *30th aerospace sciences meeting and exhibit*, 1992, p. 439.
- [3] T. J. Hughes, G. R. Feijóo, L. Mazzei, and J.-B. Quincy, “The variational multiscale method—a paradigm for computational mechanics,” *Computer methods in applied mechanics and engineering*, vol. 166, no. 1-2, pp. 3–24, 1998.
- [4] M. Milano and P. Koumoutsakos, “Neural network modeling for near wall turbulent flow,” *Journal of Computational Physics*, vol. 182, no. 1, pp. 1–26, 2002.
- [5] C. J. Lapeyre, A. Misdariis, N. Cazard, D. Veynante, and T. Poinot, “Training convolutional neural networks to estimate turbulent sub-grid scale reaction rates,” *Combustion and Flame*, vol. 203, pp. 255–264, 2019.
- [6] K. Fukami, Y. Nabae, K. Kawai, and K. Fukagata, “Synthetic turbulent inflow generator using machine learning,” *Physical Review Fluids*, vol. 4, no. 6, p. 064603, 2019.
- [7] Z. J. Zhang and K. Duraisamy, “Machine learning methods for data-driven turbulence modeling,” in *22nd AIAA Computational Fluid Dynamics Conference*, 2015, p. 2460.
- [8] J. N. Kutz, “Deep learning in fluid dynamics,” *Journal of Fluid Mechanics*, vol. 814, pp. 1–4, 2017.
- [9] K. Fukami, K. Fukagata, and K. Taira, “Super-resolution reconstruction of turbulent flows with machine learning,” *Journal of Fluid Mechanics*, vol. 870, pp. 106–120, 2019.
- [10] C. Dong, C. C. Loy, K. He, and X. Tang, “Image super-resolution using deep convolutional networks,” *IEEE transactions on pattern analysis and machine intelligence*, vol. 38, no. 2, pp. 295–307, 2015.
- [11] Y. Tai, J. Yang, and X. Liu, “Image super-resolution via deep recursive residual network,” in *Proceedings of the IEEE conference on computer vision and pattern recognition*, 2017, pp. 3147–3155.
- [12] B. Lim, S. Son, H. Kim, S. Nah, and K. Mu Lee, “Enhanced deep residual networks for single image super-resolution,” in *Proceedings of the IEEE conference on computer vision and pattern recognition workshops*, 2017, pp. 136–144.
- [13] C. Dong, C. C. Loy, and X. Tang, “Accelerating the super-resolution convolutional neural network,” in *European conference on computer vision*. Springer, 2016, pp. 391–407.
- [14] C. Ledig, L. Theis, F. Huszár, J. Caballero, A. Cunningham, A. Acosta, A. Aitken, A. Tejani, J. Totz, Z. Wang *et al.*, “Photo-realistic single image super-resolution using a generative adversarial network,” in *Proceedings of the IEEE conference on computer vision and pattern recognition*, 2017, pp. 4681–4690.
- [15] I. Goodfellow, J. Pouget-Abadie, M. Mirza, B. Xu, D. Warde-Farley, S. Ozair, A. Courville, and Y. Bengio, “Generative adversarial nets,” *Advances in neural information processing systems*, vol. 27, 2014.
- [16] Z. Deng, C. He, Y. Liu, and K. C. Kim, “Super-resolution reconstruction of turbulent velocity fields using a generative adversarial network-based artificial intelligence framework,” *Physics of Fluids*, vol. 31, no. 12, p. 125111, 2019.
- [17] W. Xu, W. Luo, Y. Wang, and Y. You, “Data-driven three-dimensional super-resolution imaging of a turbulent jet flame using a generative adversarial network,” *Applied Optics*, vol. 59, no. 19, pp. 5729–5736, 2020.
- [18] A. Subramaniam, M.-L. Wong, R. Borker, S. Nimmagadda, and S. Lele, “Turbulence enrichment with physics-informed generative adversarial network.”
- [19] A. Pradhan and K. Duraisamy, “Variational multi-scale super-resolution: A data-driven approach for reconstruction and predictive modeling of unresolved physics,” *arXiv preprint arXiv:2101.09839*, 2021.
- [20] M. Lee, N. Malaya, and R. D. Moser, “Petascale direct numerical simulation of turbulent channel flow on up to 786k cores,” in *SC’13: Proceedings of the International Conference on High Performance Computing, Networking, Storage and Analysis*. IEEE, 2013, pp. 1–11.

- [21] C. Frogner, C. Zhang, H. Mobahi, M. Araya-Polo, and T. Poggio, "Learning with a wasserstein loss," *arXiv preprint arXiv:1506.05439*, 2015.